

RESEARCH ARTICLE

Open Access



Differentiation of Pseudoprogression from True Progression in Glioblastoma Patients after Standard Treatment: A Machine Learning Strategy Combined with Radiomics Features from T₁-weighted Contrast-enhanced Imaging

Ying-Zhi Sun^{1†}, Lin-Feng Yan^{1†}, Yu Han¹, Hai-Yan Nan¹, Gang Xiao¹, Qiang Tian¹, Wen-Hui Pu², Ze-Yang Li², Xiao-Cheng Wei³, Wen Wang^{1*} and Guang-Bin Cui^{1*}

Abstract

Background: Based on conventional MRI images, it is difficult to differentiate pseudoprogression from true progression in GBM patients after standard treatment, which is a critical issue associated with survival. The aim of this study was to evaluate the diagnostic performance of machine learning using radiomics model from T₁-weighted contrast enhanced imaging (T₁CE) in differentiating pseudoprogression from true progression after standard treatment for GBM.

Methods: Seventy-seven GBM patients, including 51 with true progression and 26 with pseudoprogression, who underwent standard treatment and T₁CE, were retrospectively enrolled. Clinical information, including sex, age, KPS score, resection extent, neurological deficit and mean radiation dose, were also recorded collected for each patient. The whole tumor enhancement was manually drawn on the T₁CE image, and a total of texture 9675 features were extracted and fed to a two-step feature selection scheme. A random forest (RF) classifier was trained to separate the patients by their outcomes. The diagnostic efficacies of the radiomics model and radiologist assessment were further compared by using the accuracy (ACC), sensitivity and specificity.

Results: No clinical features showed statistically significant differences between true progression and pseudoprogression. The radiomic classifier demonstrated ACC, sensitivity, and specificity of 72.78% (95% confidence interval [CI]: 0.45, 0.91), 78.36% (95% CI: 0.56, 1.00) and 61.33% (95% CI: 0.20, 0.82). The accuracy, sensitivity and specificity of three radiologists' assessment were 66.23% (95% CI: 0.55, 0.76), 61.50% (95% CI: 0.43, 0.78) and 68.62% (95% CI: 0.55, 0.80); 55.84% (95% CI: 0.45, 0.66), 69.25% (95% CI: 0.50, 0.84) and 49.13% (95% CI: 0.36, 0.62); 55.84% (95% CI: 0.45, 0.66), 69.23% (95% CI: 0.50, 0.84) and 47.06% (95% CI: 0.34, 0.61), respectively.

Conclusion: T₁CE-based radiomics showed better classification performance compared with radiologists' assessment. The radiomics model was promising in differentiating pseudoprogression from true progression.

*Correspondence: 40204024@qq.com; cgbtd@126.com

[†]Ying-Zhi Sun and Lin-Feng Yan contributed equally to this work

¹ Department of Radiology and Functional and Molecular Imaging Key Lab of Shaanxi Province, Tangdu Hospital, Air Force Medical University, 569 Xinsi Road, Xi'an 710038, Shaanxi, China

Full list of author information is available at the end of the article



Keywords: Glioblastoma, MRI, Pseudoprogression, Radiomics, Texture feature, Machine learning

Background

Glioblastoma multiforme (GBM) is the most common primary malignant brain tumor in adults. Although maximal safe surgical resection followed by concurrent chemoradiotherapy (CCRT) with temozolomide (TMZ) and adjuvant TMZ has been a standard treatment, the prognosis of GBM patients is still very poor. Specially, the median overall survival ranges from 14 to 16 months, and the 2-year survival rate is only 26–33% [1, 2]. To improve this situation, the early and accurate diagnosis of postoperative progression has become very critical because it can directly influence the optimal therapy scheme selection associated with patient survival.

However, the pseudoprogression is a treatment-related change within 12 weeks after the completion of CCRT, including inflammation, radiation effects, ischemia and increased vascular permeability and contrast enhancement on MR imaging [3]. Both the true progression and pseudoprogression exhibit progressive enlargement and new enhancement within the radiation field. It is also difficult to differentiate them with conventional MRI sequences because pseudoprogression can mimic true progression in terms of tumor location, morphology, and enhancement patterns [4]. However, their treatments and prognosis are completely different [5]. Generally, pseudoprogression shows better outcomes and overall survival without invasive treatment [2]. According to the Response Assessment in Neuro-Oncology (RANO) criteria [3], the current strategy to distinguish pseudoprogression from true progression heavily depends on continuous follow-up MRI examinations. Where, it may take several months to obtain a reliable diagnosis, resulting in the delay or inappropriate management of progressed GBM patients [6]. Moreover, studies by Ellington et al. [7] have shown that once tumor recurrence occurs, there is no consensus on its treatment standard. Then, even if the most aggressive treatment is adopted, it is expected that there will be no significant survival benefit. Therefore, it is crucial to develop an effective method to differentiate pseudoprogression from true progression as early as possible.

Although advanced MR imaging techniques, including diffusion-weighted imaging (DWI), perfusion-weighted imaging e.g. arterial spin labeling (ASL), dynamic contrast-enhanced MRI (DCE) and dynamic susceptibility contrast perfusion MRI (DSC) and magnetic resonance spectroscopy (MRS), have been demonstrated to be promising in differentiating pseudoprogression from true progression, there are still limitations for them. First,

the lesions were measured on the basis of a single slice region of interest (ROI) or the hot-spot method, leading to the incomplete assessment of tumors [8, 9]. Second, the limited image information applied in these studies cannot fully address tumor heterogeneity. Third, excessive parameters and time-consuming post-processing limit their clinical applications [10, 11]. Besides, advanced sequences highly depend on the performance of the scanner and are not available in all hospitals. Thus, it is urgent to develop a user-friendly protocol for the early and comprehensive differentiation of pseudoprogression from true progression.

Recently, the term radiomics, by extracting a large number of quantitative image features combined with machine learning algorithms, radiomics can provide information that is difficult to perceive by visual inspection to guide clinical decision-making, has attracted increased attention in the medical field, especially in tumor research for diagnosis, staging and prognosis [12–15]. The radiomics strategy has also been used to identify pseudoprogression and true progression [16–18]. However, most of them were largely focused on advanced MR techniques, and the varied post-processing models, varied interpretation and uniform standards for evaluation restricted their clinical applications. In contrast, T₁CE is widely used in almost all hospitals for the diagnosis and follow-up of GBM patients. Thus, developing an effective T₁CE based radiomics model to differentiate pseudoprogression and true progression will have great potential in clinic.

In this study, we aimed to evaluate the diagnostic power of T₁CE imaging radiomics-based machine learning in differentiating pseudoprogression from true progression in GBM patients after standard treatment. The diagnostic power of radiomics model was further compared with that of radiologists' assessment.

Methods

Patient population

This study was approved by our institutional review board, and the requirement for informed consent was waived based on its retrospective nature. One hundred thirty-one pathologically confirmed primary GBM patients were retrospectively enrolled from May 2014 to February 2017 in Tangdu hospital.

The inclusion criteria were as follows: (1) GBM patients underwent gross total resection or subtotal resection of the lesion; (2) routine MRI was performed within 48 h after surgery, including T₁-weighted imaging (T₁WI)

and contrast-enhanced T_1 WI; (3) the patients underwent standard treatment (CCRT with TMZ and six cycles of adjuvant TMZ after surgery); (4) the patients underwent a second round of MR imaging within 2 months after CCRT with TMZ, and the third follow-up MRI examination was obtained at 6 months after CCRT [19]; (5) the patients did not receive corticosteroid treatment 3 days before each MRI examination; (6) the patients had new or enlarged enhancement within the radiation field on the second follow-up MR images; and (7) the patients were confirmed to have true progression or pseudoprogression through pathology after the second surgery or clinical radiologic follow-up.

Fifty-four patients were excluded for the following reasons: (1) absence of new or enlarged enhancement at the end of radiation therapy with concurrent TMZ ($n=15$); (2) lack of standardized treatment schedules after surgery ($n=10$); (3) poor image quality or motion artifacts ($n=11$); and (4) lack of complete clinical radiological follow-up or pathological evidence ($n=18$).

Finally, 77 patients were included and confirmed to have true progression ($n=51$) or pseudoprogression ($n=26$). Thirteen patients with true progression and 2 patients with pseudoprogression were confirmed by pathology of the reoperation samples. The other 2 patients died of GBM-related complications within 9 months and were also classified into the true progression group. The other patients with true progression ($n=36$) or pseudoprogression ($n=24$) according to the RANO criteria [3]. The details of the patient enrollment are shown in Fig. 1.

Image Acquisition

The MRI protocol was performed on a 3.0 T MRI scanner (MR750, GE Healthcare, and Milwaukee, Wisconsin, USA) with an 8-channel head coil (General Electric Medical System). Preoperative and the follow-up MR images were collected including axial T_1 -weighted imaging (T_1 WI), T_2 -weighted imaging (T_2 WI), fluid-attenuated inversion recovery (FLAIR) and T_1 -weighted contrast-enhanced imaging (T_1 CE).

The scanning parameters were as follows: axial T_1 WI (TR/TE, 1750 ms/24 ms; matrix size, 256×256 ; FOV, 24×24 cm; number of excitations (NEX), 1; slice thickness, 5 mm; and gap, 1.5 mm), axial T_2 WI (TR/TE, 4247 ms/93 ms; matrix size, 512×512 ; FOV, 24×24 cm; NEX, 1; slice thickness, 5 mm; and gap, 1.5 mm), sagittal T_2 WI (TR/TE, 4338 ms/96 ms; matrix size, 384×384 ; FOV, 24×24 cm; NEX, 2; slice thickness, 5 mm; and gap, 1.0 mm), and axial FLAIR (TR/TE, 8000 ms/165 ms; matrix size, 256×256 ; FOV, 24×24 cm; NEX, 1; slice thickness, 5 mm; and gap, 1.5 mm). Finally, a contrast-enhanced T_1 -weighted spin-echo sequence was acquired

in the transverse, sagittal, and coronal planes after intravenous administration of 0.1 mmol/kg gadodiamide (Omniscan; GE Healthcare, Co., Cork, Ireland).

Segmentation of the volume of interest (VOI)

The research pipeline, including image preprocessing, feature extraction, feature selection and radiomics model building is depicted in Fig. 2. Two neuroradiologists (L.F.Y., with 12 years of experience and Y.Z.S., with 10 years of experience in neuro-oncology imaging) independently reviewed all images. A third senior neuroradiologist (G.B.C., with 25 years of experience in brain tumor imaging) re-examined the images and determined the final classification when inconsistencies existed between the two neuroradiologists. In assessing whether the lesion progressed after complete resection, the preoperative image features of the tumor would affect the results. Thus, the preoperative image features of the tumor were also observed and characterized based on the criteria outlined in Additional file 1: Table S1.

The VOIs were semi-automatically segmented by the two neuroradiologists (L.F.Y. and Y.Z.S.) using ITK-SNAP (version 3.6, <http://www.itk-snap.org>). The VOIs covering the enhanced lesion were drawn slice by slice on T_1 CE, avoiding the regions of macroscopic necrosis, cystic, edema and non-tumor macrovessels, at the second follow-up MR imaging within 2 months after standard treatment [20].

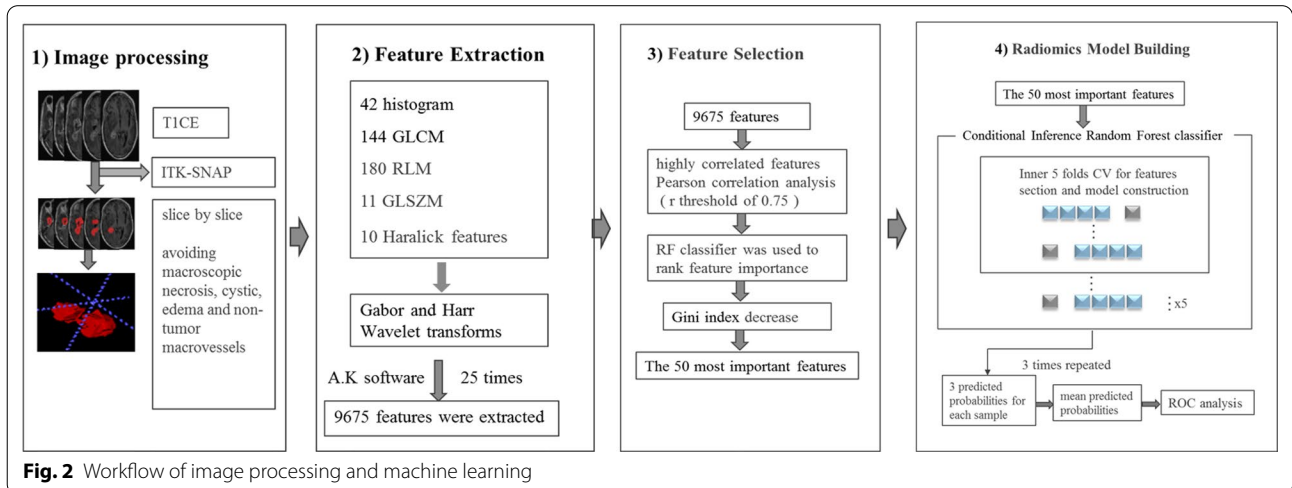
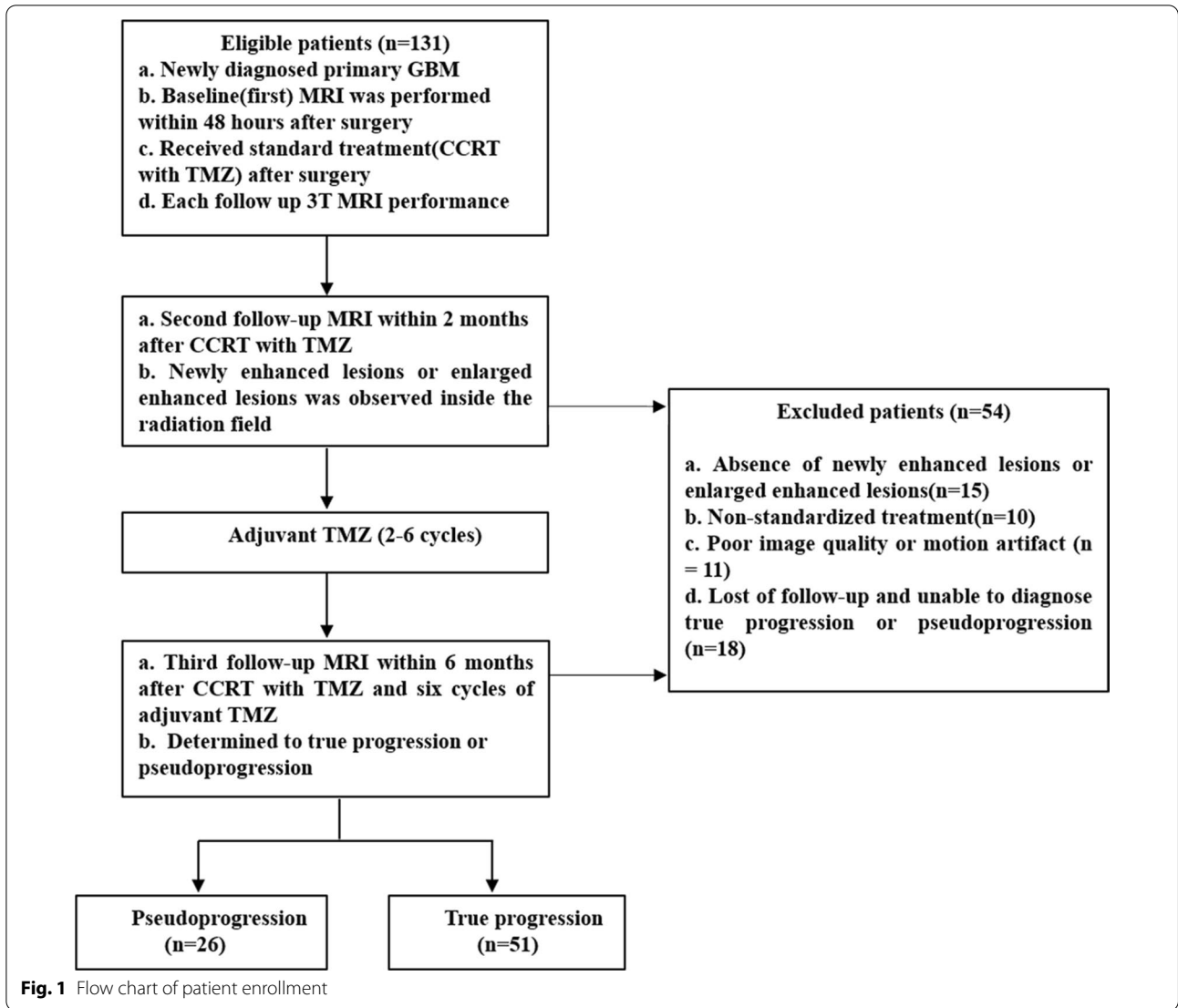
Radiomics Strategy

Feature Extraction

A series of texture features were involved in this study, including 42 histogram features, 11 Gy level size zone matrix (GLSZM) texture features, 10 Haralick features, 144 Gy level co-occurrence matrix (GLCM) texture features and 180 run-length matrix (RLM) texture features of the original images. The after 25 times Gabor and Haar wavelet transforming. Then, a total of 9675 features were extracted from the T_1 CE images using Analysis-Kinetics (A.K., GE Healthcare) software. The aforementioned features were used here because they were found to be relevant for distinguishing glioma grades in our previous study [14].

Feature Selection

After normalization, the highly redundant and correlated features were subjected to a two-step feature selection procedure. First, highly correlated features were eliminated using Pearson correlation analysis, with an threshold of 0.75. Then, a random forest (RF) classifier consisting of a number of decision trees was used to rank the feature importance. Specially, each node in the decision trees is a condition on a single feature, designed



to split the dataset into two and similar response values will end up in the same set. The measurement based on which the (locally) optimal condition is determined is called impurity. When training a tree, how much each feature decreases this weighted impurity in the tree can be computed. Furthermore, for a forest, the impurity decrease of each feature can be averaged across the trees, and then used to rank the features, i.e. feature importance. In our study, the Gini impurity decrease was used as the criterion to evaluate the feature importance for feature selection.

Radiomics Model Building

After feature ranking, the 50 most important features were fed into a conditional inference RF classifier for model fitting [21]. The synthetic minority oversampling technique (SMOTE) strategy was used to address the data imbalance issue [22]. Five-fold cross validation method was employed for tuning the hyperparameter and performed 3 times to avoid bias and overfitting as much as possible. Then these results were averaged to get the final performance.

The accuracy, sensitivity and specificity of the receiver operating characteristic (ROC) were computed to evaluate the constructed radiomics model.

Radiologists' assessment

To compare the efficacies of radiologists' assessment and radiomics model in differentiating pseudoprogression from true progression, the images were also evaluated by three junior neuroradiologists (Q.T., G.X. and Y.H., with 8, 7 and 7 years of experience in neuroradiology, respectively) using the second follow-up MR images when new or enlarged enhanced lesions were observed within the radiation field. The neuroradiologists were blinded to the clinical information but were aware that the tumors showed either pseudoprogression or true progression, without knowing the exact category each patient fell in. Each reader independently assessed only the T₁CE images and recorded a final diagnosis using a 4-point scale (1 = definite pseudoprogression; 2 = likely pseudoprogression; 3 = likely true progression; and 4 = definite true progression) [23].

Statistics

For comparisons of the differences in clinical characteristics between the pseudoprogression and true progression groups, Fisher's exact test or the chi-square test was used for the categorical variables, and unpaired Student's t test was used for continuous variables. These were performed by using SPSS 20.0 software (SPSS Inc., Chicago, IL, USA). *P* value < 0.05 was considered to indicate statistical significance.

Radiomics model construction was performed using R version 3.4.2 (R Foundation for Statistical Computing). The 'RF' and 'caret' packages were used for feature selection and SMOTE, respectively. The diagnostic performance of the radiomics model was assessed by using the accuracy, sensitivity, specificity. The same values of the three readers for differentiating pseudoprogression from true progression were also calculated and compared with the radiomics model.

Results

Patient Characteristics and Qualitative MR Assessment

The patient characteristics are summarized in Table 1. The study group consisted of 40 men and 37 women with a mean age of 49.1 ± 10.5 years (range 17–76 years). The symptoms of these patients included headache and vomiting (61.0%; 47 of 77 patients), epilepsy (18.2%; 14 of 77), physical dysfunction (20.8%; 16 of 77) and others (31.1%; 24 of 77). None of the pretreatment clinical characteristics, including sex, age, Karnofsky Performance Status (KPS) score, resection extent, neurological deficit and mean radiation dose, showed significant difference in differentiating pseudoprogression from true progression.

In addition, the diagnostic powers of preoperative image features in differentiating pseudoprogression from true progression were summarized in Additional file 1: Table S2. The side of the tumor exhibited statistically significant (*P* = 0.023), and the location of the tumor had a tendency towards statistical significance between-group difference (*P* = 0.053).

Figures 3 and 4 demonstrate representative patients with pseudoprogression and true progression on T₁CE imaging, respectively. The pseudoprogression case (Fig. 3), in the absence of more interventions, showed a strengthened extent of the lesion and a reduced degree of enhancement. The case of true progression (Fig. 4) showed a marked increase in the extent of the enhanced lesions, which was confirmed by secondary surgical pathology as tumor recurrence.

Quantitative MR Texture Analysis

Figure 5 depicts the relative importance of the top 50 features based on the Gini index. In the present study, 92% (*n* = 46) of the key features in the radiomics model were wavelet features. Twenty-two of the top 50 texture features had significant differences between the true progression group and the pseudoprogression group (Table 2).

These optimal features included 1 GLSZM texture feature, 6 histogram texture features, 19 GLCM texture features and 24 RLM texture features. The details of the optimal feature subsets are provided in Additional file 1:

Table 1 Clinical characteristics of patients

Variable	Total	Pseudoprogression	True progression	P value
No. of patients	77	n = 26	n = 51	NA
Gender				
Male	40	12 (46.2%)	28 (54.9%)	0.482*
Female	37	14 (53.8%)	23 (45.1%)	
Age				
Mean	49.1 ± 10.5	47.1 ± 10.2	50.1 ± 10.4	0.230**
Karnofsky Performance Scale Score				
≤ 80	36	11 (89.3%)	25 (98.9%)	0.635*
> 80	41	15 (10.7%)	26 (1.1%)	
Surgery				
Subtotal resection	17	5 (29.4%)	12 (70.6%)	0.776*
Gross total resection	60	21 (35%)	39 (65%)	
Neurological Deficit				
No	44	16 (36.4%)	28 (63.6%)	0.633*
Yes	33	10 (30.3%)	23 (69.7%)	
Mean Radiation Dose(Gy)	59.1	59.5	58.6	0.365*

Except where indicated, data are numbers of patients

^a Data are mean ± standard deviation

*Calculated by using the Fisher's exact test. **Calculated by using unpaired Student t test

The difference between the groups was significant ($P < 0.05$)

Table S3. The RLM texture features accounted for the highest proportion of the top 50 features, among which Short Run Emphasis_angle45_offset1_LHHL was the most relevant feature and was significantly lower in patients with true progression than in patients with pseudoprogression (Table 2). The GLCM texture feature was the second most dominant feature computed from T₁CE (Fig. 5) and was significantly higher in patients with pseudoprogression than in patients with true progression (Table 2). The histogram feature and GLSZM texture feature were the least relevant of the top 50 features. Skewness_LHLH and low intensity small area emphasis were the fourth and ninth most relevant features (Fig. 5) and were significantly lower in patients with true progression than in patients with pseudoprogression (Table 2). Low intensity small area emphasis indicated that hypointense zones were more likely to be present in pseudoprogression patients. The above results indicated that lesions with a relatively homogenous appearance were associated with pseudoprogression.

The optimal performance was obtained by using an RF classifier trained with 50 trees. The RF classifier achieved an ACC of 72.78% (95% confidence interval [CI]: 0.45, 0.91) for differentiating pseudoprogression from true progression, with a sensitivity of 78.36% (95% CI: 0.56, 1.00), and a specificity of 61.33% (95% CI: 0.20, 0.82) (Table 3).

Comparison of the diagnostic performance between the radiomics model and the radiologists' assessment

Table 3 showed the comparison of the diagnostic performance of the radiomics model and the radiologists' assessment using the same T₁CE image data. The accuracy, sensitivity and specificity of three radiologists' assessment were 66.23% (95% CI: 0.55, 0.76), 61.50% (95% CI: 0.43, 0.78) and 68.62% (95% CI: 0.55, 0.80); 55.84% (95% CI: 0.45, 0.66), 69.25% (95% CI: 0.50, 0.84) and 49.13% (95% CI: 0.36, 0.62); 55.84% (95% CI: 0.45, 0.66), 69.23% (95% CI: 0.50, 0.84) and 47.06% (95% CI: 0.34, 0.61), respectively. In comparing the diagnostic performance, the ACC, sensitivity and specificity of the radiomics model were significantly higher than those of the three radiologists' assessment.

The ROC curve in Fig. 6 indicated that the radiomics model has better diagnostic performance than the radiologists' assessment.

Discussion

In this study, none of the pretreatment clinical characteristics showed significant difference between the two groups. In addition, according to the results of preoperative imaging characteristics analysis, only the side of the tumor was statistically significant and the location of the tumor had a tendency towards statistical significance between two groups (Additional file 1: Table S2). The

Table 2 Statistical differences of radiomic features determined by using RF classifier between pseudoprogression and true progression

Feature	Gini Importance	True progression		Pseudoprogression		p value
		Median	Interquartile range	Median	Interquartile Range	
Feature1	3.73	0.998	0.995–0.999	0.996	0.993–0.999	<.001
Feature2	2.91	1.30×10^{-5}	2.0×10^{-6} – 6.8×10^{-5}	3.39×10^{-5}	7.34×10^{-6} – 1.19×10^{-4}	<.001
Feature3	2.08	3.0×10^{-13}	1.04×10^{-14} – 4.2×10^{-12}	5.59×10^{-13}	1.26×10^{-13} – 7.91×10^{-12}	.079
Feature4	2.08	– 0.20	– 1.21–0.83	– 0.58	– 1.79–1.09	<.001
Feature5	1.98	1.14×10^4	1725.0–72,802.4	2.03×10^4	9098.51–56,899.20	.015
Feature6	1.53	3.32×10^{-4}	1.44×10^{-4} – 7.51×10^{-4}	4.65×10^{-4}	1.71×10^{-4} – 7.57×10^{-4}	<.001
Feature7	1.45	16.22	1.20–241.05	37.06	11.14–254.88	.137
Feature8	1.42	221.32	14.89–5051.62	349.15	89.95–5227.03	.765
Feature9	1.39	5.25×10^{-6}	2.45×10^{-7} – 2.04×10^{-5}	6.44×10^{-7}	2.43×10^{-7} – 8.2×10^{-6}	.828
Feature10	1.32	5.35×10^8	2.20×10^7 – 1.64×10^{11}	2.34×10^9	1.85×10^8 – 9.06×10^{10}	.374
Feature11	1.25	4.84×10^{-5}	1.3×10^{-5} – 1.96×10^{-4}	7.3×10^{-5}	5.74×10^{-6} – 1.75×10^{-4}	.008
Feature12	1.25	14.49	1.08–342.81	35.44	2.47–189.35	.244
Feature13	1.24	– 2393.65	– 61,416.60–36,264.10	– 1.26×10^4	– 152×10^5 – 5.76×10^4	.015
Feature14	1.09	1.5×10^{-13}	5.05×10^{-15} – 8.51×10^{-9}	2.72×10^{-13}	8.2×10^{-14} – 1.83×10^{-11}	.445
Feature15	1.07	1.8×10^{-5}	1.22×10^{-6} – 7.55×10^{-5}	2.8×10^{-5}	5.75×10^{-6} – 1.08×10^{-4}	.005
Feature16	1.01	0.998	0.994–0.999	0.996	0.993–0.999	<.001
Feature17	0.93	3.27×10^{-5}	– 3.14×10^{-4} – 7.18×10^{-4}	1.47×10^{-4}	– 5.47×10^{-4} – 4.69×10^{-4}	.050
Feature18	0.93	– 744.67	– 1.68×10^4 – 1.03×10^4	748.24	– 11,634.40–18,560.10	.138
Feature19	0.89	0.12	1.91×10^{-4} –8.93	0.14	5.95×10^{-4} –5.43	.197
Feature20	0.82	0.55	0.35–0.66	0.56	0.50–0.73	.028
Feature21	0.81	1.3×10^{-13}	1.20×10^{-14} – 2.97×10^{-12}	2.52×10^{-13}	5.05×10^{-14} – 2.07×10^{-9}	.161
Feature22	0.76	1.83×10^9	6.18×10^7 – 7.80×10^{10}	6.48×10^9	7.02×10^8 – 9.28×10^{10}	.048
Feature23	0.75	0.998	0.994–0.999	0.997	0.994–0.998	.256
Feature24	0.74	0.998	0.994–1.000	0.998	0.997–0.999	.347
Feature25	0.73	5.1×10^{-12}	1.53×10^{13} – 4.33×10^{10}	1.44×10^{-11}	1.17×10^{-12} – 3.16×10^{-8}	.141
Feature26	0.72	1.73×10^{-4}	– 2.99×10^{-4} – 7.68×10^{-4}	1.69×10^{-4}	3.13×10^{-6} – 7.69×10^{-4}	.060
Feature27	0.71	3.72×10^{-4}	2.19×10^{-4} – 1.06×10^{-3}	4.43×10^{-4}	3.16×10^{-4} – 1.04×10^{-3}	.006
Feature28	0.70	7.47×10^3	999.18–41,102.90	1.16×10^4	1287.42–25,000.80	.111
Feature29	0.69	– 342.35	– 4559.64–8392.05	672.42	– 8078.63–28,881.70	.208
Feature30	0.68	– 1.02×10^3	– 5065.29–1823.32	– 600.96	– 2031.27–3107.47	.125
Feature31	0.66	6.80×10^8	2.59×10^7 – 1.87×10^{10}	2.12×10^9	3.88×10^7 – 3.44×10^{11}	.103
Feature32	0.65	843.33	160.59–1046.56	753.13	258.74–1333.93	.147
Feature33	0.62	– 9.8×10^{-5}	– 5.9×10^{-4} – 3.22×10^{-4}	– 8.60×10^{-5}	– 3.36×10^{-4} – 1.4×10^{-4}	.799
Feature34	0.62	967.43	69.37–6660.59	2441.03	149.65–10,040.5	.002
Feature35	0.60	5.83×10^{-6}	1.51×10^{-6} – 1.89×10^{-5}	8.91×10^{-6}	2.43×10^{-6} – 2.95×10^{-5}	.015
Feature36	0.58	1.69×10^4	9790.15–26,645.1	18,893.30	13,895.80–32,379.50	.008
Feature37	0.58	1.99×10^{-4}	– 3.4×10^{-4} – 8.7×10^{-4}	2.87×10^{-4}	– 7.65×10^{-5} – 1.44×10^{-3}	.060
Feature38	0.53	– 467.89	– 3.00×10^4 – 1.79×10^4	799.64	– 35,322.10–20,325.90	.575
Feature39	0.53	4.95×10^{-9}	1.34×10^{-9} – 1.60×10^{-8}	5.83×10^{-9}	5.38×10^{-10} – 3.45×10^{-8}	.037
Feature40	0.53	14.17	– 5.15×10^3 – 1.25×10^4	– 939.69	– 27,364.50–5113.09	.026
Feature41	0.52	– 259.96	– 16,902.50–9521.71	1264.01	– 10,087.90–6781.62	.121
Feature42	0.52	– 1.20	– 2.52–0.10	– 0.81	– 2.07–0.20	.043
Feature43	0.52	2.22	0.30–12.95	2.76	1.54–5.43	.536
Feature44	0.52	9.53×10^{10}	1.10×10^{10} – 4.10×10^{12}	2.30×10^{11}	4.82×10^9 – 7.26×10^{12}	.023
Feature45	0.52	1.04×10^5	2.21×10^4 – 5.96×10^5	1.40×10^5	37,793.10–516,907.00	.025
Feature46	0.52	3.30×10^5	1.23×10^5 – 2.56×10^6	4.29×10^5	1.27×10^5 – 1.39×10^6	.505
Feature47	0.51	9.1×10^{-14}	9.09×10^{-14} – 9.42×10^{-15}	1.96×10^{13}	4.65×10^{-14} – 8.41×10^{-13}	.110
Feature48	0.50	0.51	0.39–0.64	0.48	0.38–0.62	.074
Feature49	0.49	6.27×10^{-7}	5.39×10^{-8} – 4.22×10^{-6}	1.37×10^{-6}	1.71×10^{-7} – 4.76×10^{-6}	.005
Feature50	0.49	– 4.9×10^{-3}	– 0.55–0.50	0.06	– 0.68–0.63	.414

Table 2 (continued)

Feature relevance was assessed by using mean decrease in Gini index–based feature importance

P values are adjusted for false-discovery rate by using Benjamini–Hochberg method. 1–50 features are the same as in Fig. 4

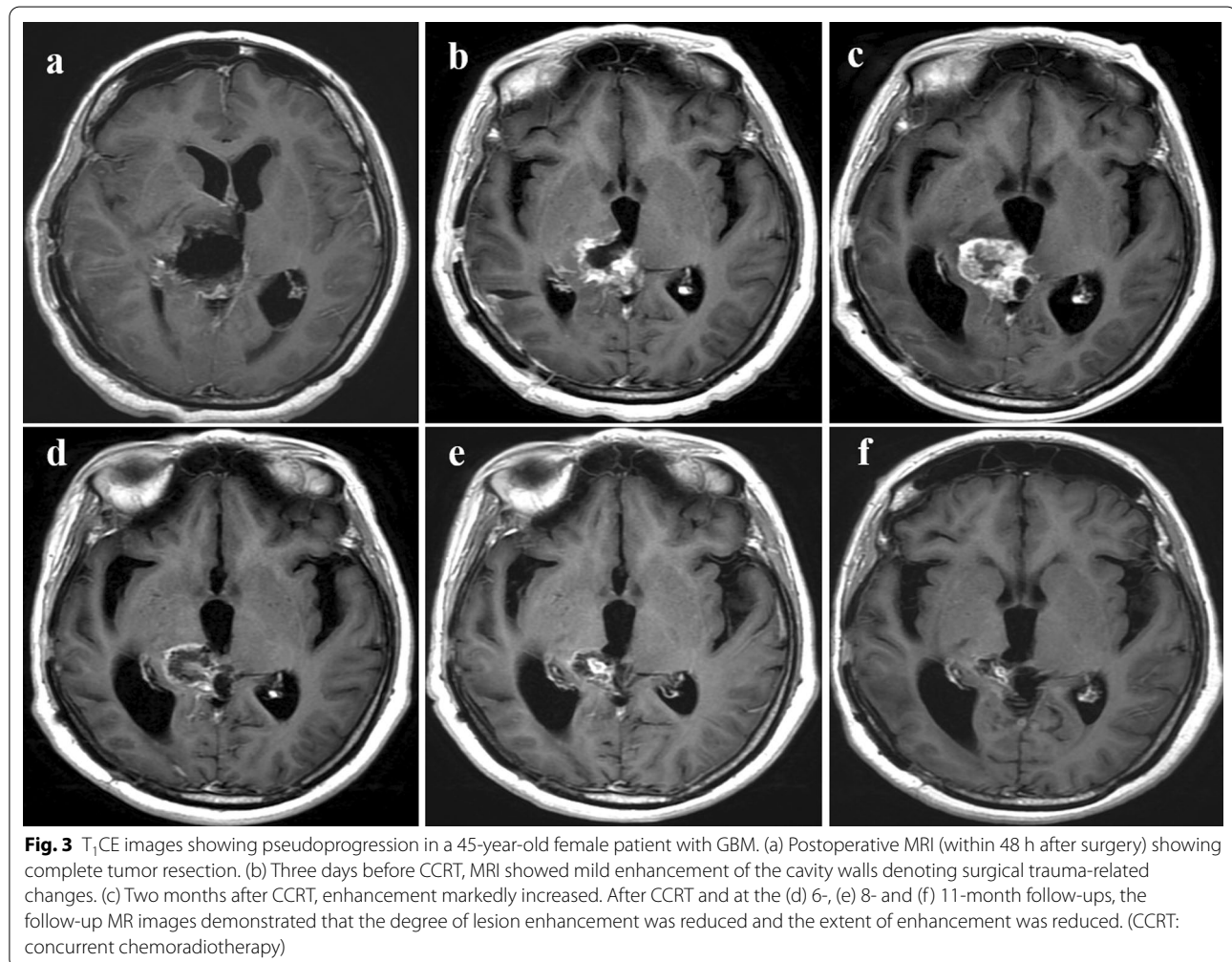


Fig. 3 T₁CE images showing pseudoprogression in a 45-year-old female patient with GBM. (a) Postoperative MRI (within 48 h after surgery) showing complete tumor resection. (b) Three days before CCRT, MRI showed mild enhancement of the cavity walls denoting surgical trauma-related changes. (c) Two months after CCRT, enhancement markedly increased. After CCRT and at the (d) 6-, (e) 8- and (f) 11-month follow-ups, the follow-up MR images demonstrated that the degree of lesion enhancement was reduced and the extent of enhancement was reduced. (CCRT: concurrent chemoradiotherapy)

results may be related to the small sample size and data imbalance, we will observe the results in future research.

The ability of quantitative radiomics features based on T₁CE images to differentiate pseudoprogression from true progression in patients with GBM after CCRT was investigated in the current study. When combined with RF classifier, the radiomics model achieved relatively good diagnosis performance with higher ACC (72.78%) and sensitivity (78.36%) than radiologists' assessment.

Regarding the top 50 most important features selected by using the Gini index as a metric, most of them were RLM ($n=24$) and GLCM ($n=19$) features. The RLM mainly reflects the roughness and directionality of the texture. The GLCM reflects the intensity of the

spatial distribution [24]. The histogram features ($n=6$) and GLSZM texture feature ($n=1$) were also played an important role in identifying pseudoprogression and true progression. The ninth important feature of low intensity small area emphasis indicated that hypointense zones were more likely to be present in pseudoprogression patients. Previous literature reports have shown that low intensity small area emphasis may reflect fibrinoid necrosis, oligodendroglial injury and glial cell hyperplasia [11, 25]. The higher the value was the greater the probability of pseudoprogression, which appears as a low-signal region. On the contrast, recurrent GBM was characterized by vascular proliferation and a disrupted blood–brain barrier, leading to the high signal intensity in the T₁CE image

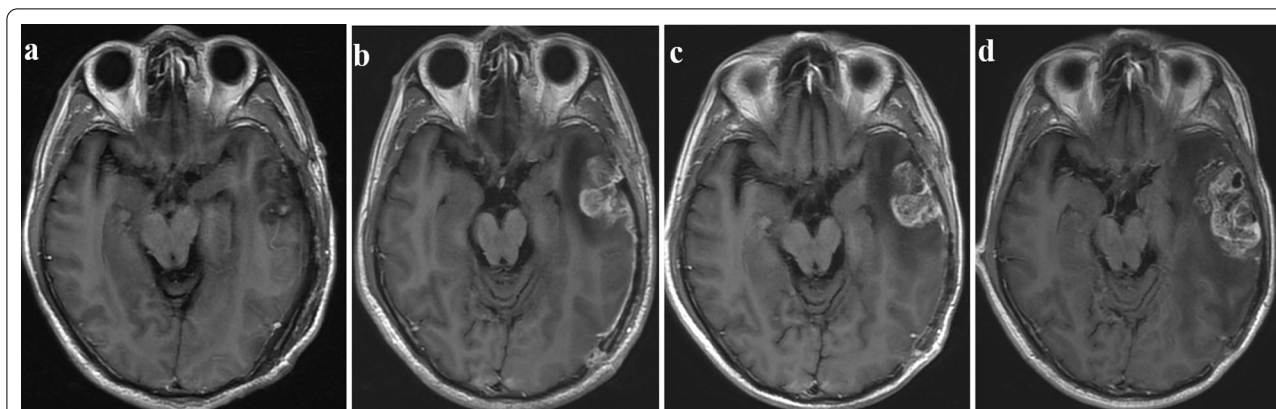


Fig. 4 T₁CE images showing true progression in a 48-year-old male patient with GBM. (a) Postoperative MRI (within 24 h after surgery) showed that the tumor was completely resected. (b) Two months after CCRT, the new enhancement disappeared. After CCRT and at the (c) 6- and (d) 9-month follow-ups, the follow-up MR images demonstrated that the extension of the enhanced lesion increased. Recurrence was confirmed by second surgical pathology. (GBM: glioblastoma multiforme)

caused by contrast agent leakage [11, 26]. Above texture features mainly reflect the tumor heterogeneity and complexity of components based on voxel-based changes in grayscale [27]. Specially, the Haralick features were not in the top 50 features, which probably suggested that these two groups of features were not effective in distinguishing pseudoprogression from true progression and needed to be verified in future research.

Moreover, it can be observed that, in our study, 92% ($n=46$) of the key features in the radiomics model were Gabor filtered wavelet features. The use of high-dimensional feature helps to improve the performance of the model. This finding demonstrates that the wavelet features can provide more information about the tumor invisible to the eye, so as to better assess treatment response [28, 29].

Previous studies have used low-dimensional features coupled with a few pieces of information from multi-parametric histograms [16] or SVM classification based on DCE MRI to differentiate pseudoprogression from true progression [30]. Although these studies achieved good results in differentiating pseudoprogression from true progression in GBM patients with standard treatment, there were still certain disadvantages. First, the samples and quantitative features in previous studies were relatively small, especially the relatively small number of pseudoprogression patients without proper handling, which might have overshadowed their statistical results [16]. Second, previous studies were mostly based on advanced MR sequences that were of much equipment dependent and may hamper its application in some primary hospitals.

To the best of our knowledge, there is no published study in the literature comparing the radiomics model

with radiologists' assessment for distinguishing pseudoprogression from true progression. In our study, the radiomics model demonstrated better diagnostic performance than the radiologists' assessment. It suggested that our radiomics model may have the potential to help clinicians make an earlier judgment for patients in whom a "wait and see" approach may be the most appropriate.

Study limitations

Several limitations of the current study should be addressed. First, the sample size was still small, so there may be a risk of overfitting. In order to solve the problem of small sample size and overfitting risk, we adopted the following methods: 1) 25 times Gabor and wavelet transformations were performed on the features extracted from the original images. 2) five-fold cross validation was employed for tuning the hyperparameter and was performed 3 times to avoid bias and overfitting as much as possible. 3) the SMOTE strategy was used to address the data imbalance issue, especially the sample size of pseudoprogression was relatively small. Moreover, Bum-Sup Jang et al. built a radiomics model by machine learning algorithm differentiating pseudoprogression from true progression with the total amount of sample they used was 78 cases [31]. In the future, a much larger dataset needs to be investigated to validate the robustness and reproducibility of the currently proposed radiomics model. Second, molecular alterations, such as isocitrate dehydrogenase (IDH) mutation and oxygen 6-methylguanine-DNA methyltransferase (MGMT) promoter methylation status, were not included in this study. The recently published 2016 WHO classification of brain tumors incorporated genetic parameters into the classical histopathological findings. These genetic alterations have

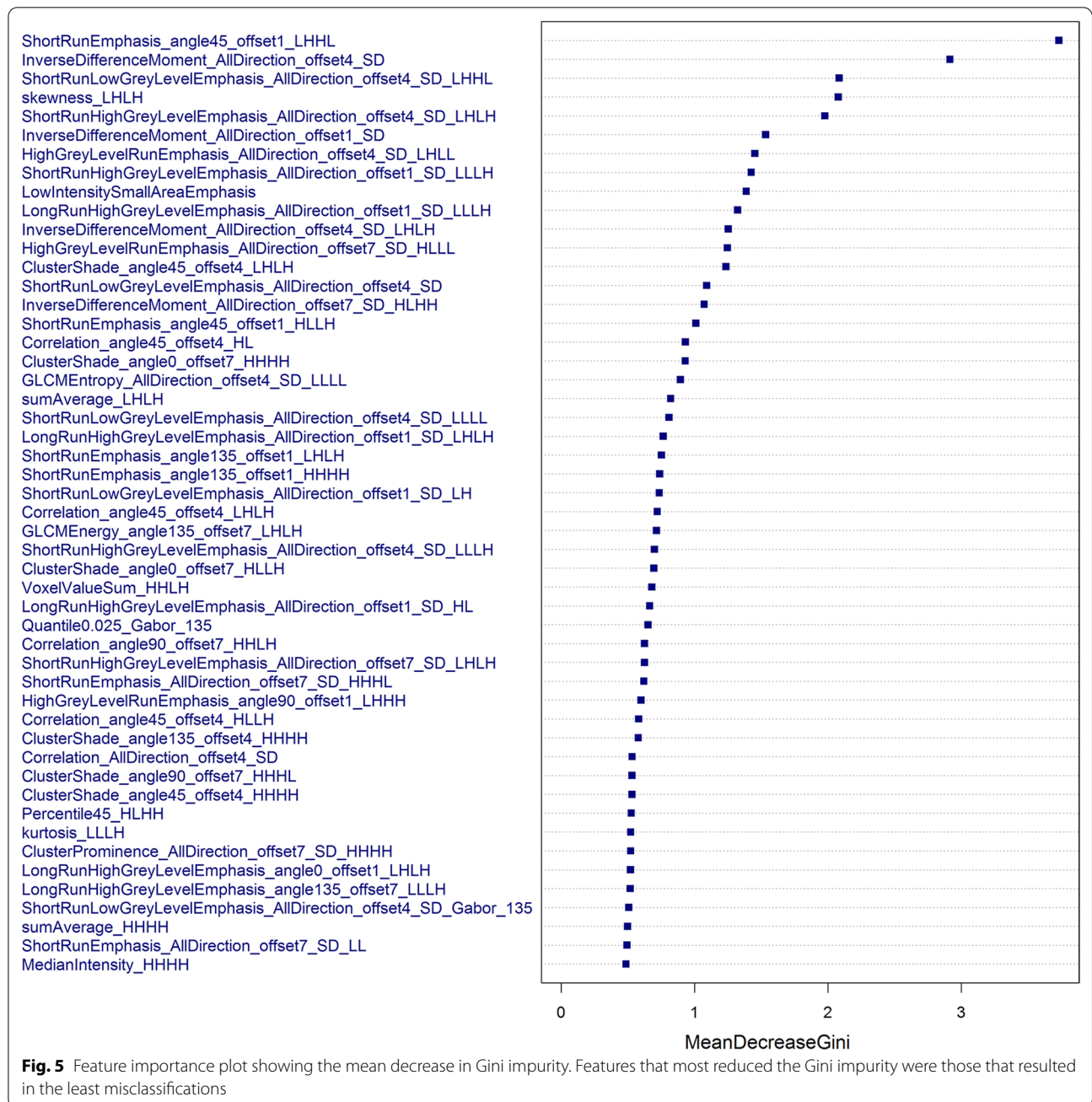
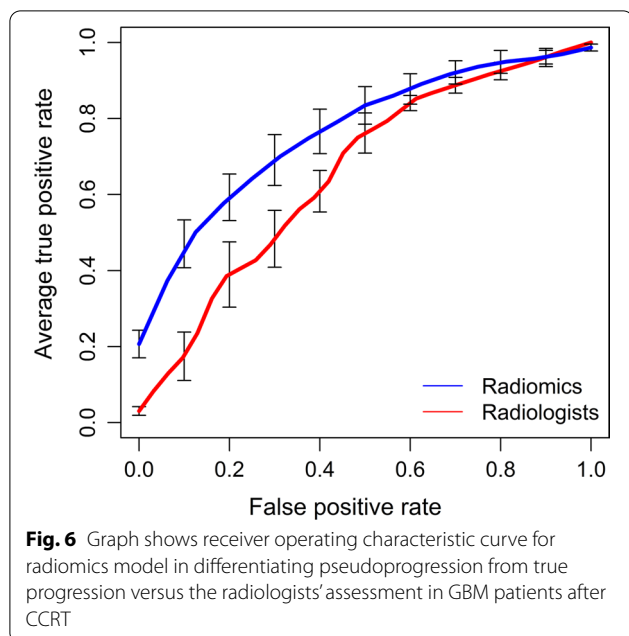


Table 3 Diagnostic performances of the radiomics model for differentiating pseudoprogession from true progression versus the radiologists' assessment

	ACC	Sensitivity	Specificity
Radiomics	72.78%(95% CI: 0.45,0.91)	78.36%(95% CI: 0.56,1.00)	61.33%(95% CI: 0.20,0.82)
Radiologist 1	66.23%(95% CI: 0.55,0.76)	61.50%(95% CI: 0.43,0.78)	68.62%(95% CI: 0.55,0.80)
Radiologist 2	55.84%(95% CI: 0.45,0.66)	69.25%(95% CI: 0.50,0.84)	49.13%(95% CI: 0.36,0.62)
Radiologist 3	55.84%(95% CI: 0.45,0.66)	69.23%(95% CI: 0.50,0.84)	47.06%(95% CI: 0.34,0.61)



prognostic implications in terms of survival and response to therapies [32, 33]. These indicators will be included in future studies.

Conclusion

In conclusion, our study showed that the proposed radiomics model based on conventional T_1 CE had stable diagnostic efficacy and performed better than the radiologists' assessment in the early differentiation of pseudoprogression from true progression in GBM patients after CCRT. The radiomics model may assist clinicians in the early, accurate judgment of recurrence and provide a novel tool to guide individual treatment strategies for GBM patients.

Supplementary Information

The online version contains supplementary material available at <https://doi.org/10.1186/s12880-020-00545-5>.

Additional file 1. Details of the preoperative image features and top 50 importance features for differentiating pseudoprogression from true progression.

Abbreviations

AUC: Area Under the Curve; ADC: Apparent Diffusion Coefficient; ASL: Arterial Spin Labeling; DCE: Dynamic Contrast Enhancement; DSC: Dynamic Susceptibility Contrast; DWI: Diffusion-weighted Imaging; GLCM: Gray-level Cooccurrence Matrix; GLSZM: Gray Level Size Zone Matrix; KPS: Karnofsky Performance Status; MGMT: O⁶-methylguanine-DNA Methyltransferase; ROC: Receiver Operating Characteristic; ROI: Region of Interest; RLM: Run-length Matrix; RF: Random Forest; SVM: Support Vector Machine; SMOTE: Synthetic Minority Oversampling Technique; T1CE: T₁-weighted Contrast-enhanced Imaging; VOI: Volume of Interest.

Acknowledgements

We would like to thank Dr. Xiao-Cheng Weiat GE Healthcare China for providing technical support regarding the application of Analysis-Kit software.

Authors' contributions

CGB and WW conceived the project; SYZ and YLF conducted the patient enrollment and data collection; HY, TQ, PWH, LZ, XG and WXC contributed to the data analysis and graph making; and NHY contributed to the thoughtful discussion and provided constructive help in the data analysis. SYZ, YLF, WW and CGB drafted the manuscript. All authors read and approved the final manuscript.

Funding

This study received financial support from the National Key Research and Development Program of China (No. 2016YFC0107105 to Dr. C.G.B.), the Innovation and Development Foundation of Tangdu Hospital (No.2016LCYJ001 to Dr. C.G.B.) and the Young Seeding Talent Foundation of Tangdu Hospital (to Dr. Y.L.F.). The funding bodies did not play any roles in the design of the study, in the collection, analysis, and interpretation of the data or in the writing of the manuscript.

Availability of data and materials

The datasets used and/or analyzed during the current study are available from the corresponding author upon reasonable request.

Ethics approval and consent to participate

The retrospective study was approved by the Air Force Medical University, Tang Du Hospital Institutional Review Board and the requirement for written informed consent was waived. (Study Nr.201510-013).

Consent for publication

Our manuscript does not contain any individual person's data. (Not applicable).

Competing interests

The authors declare no conflicts of interest.

Author details

¹ Department of Radiology and Functional and Molecular Imaging Key Lab of Shaanxi Province, Tangdu Hospital, Air Force Medical University, 569 Xinsi Road, Xi'an 710038, Shaanxi, China. ² Student Brigade, Air Force Medical University, Xi'an 710032, Shaanxi, China. ³ GE Healthcare, Shanghai 210000, China.

Received: 30 June 2020 Accepted: 28 December 2020

Published online: 03 February 2021

References

- Ostrom QT, Gittleman H, Fulop J, Liu M, Blanda R, Kromer C, Wolinsky Y, Kruchko C, Barnholtz-Sloan JS: CBTRUS Statistical Report: Primary Brain and Central Nervous System Tumors Diagnosed in the United States in 2008–2012. *Neuro Oncol* 2015, 17 Suppl 4:iv1-iv62.
- Erpolat OP, Akmansu M, Goksel F, Bora H, Yaman E, Buyukberber S: Outcome of newly diagnosed glioblastoma patients treated by radiotherapy plus concomitant and adjuvant temozolomide: a long-term analysis. *Tumori*. 2009;95(2):191–7.
- Wen PY, Macdonald DR, Reardon DA, Cloughesy TF, Sorensen AG, Galanis E, Degroot J, Wick W, Gilbert MR, Lassman AB, et al. Updated response assessment criteria for high-grade gliomas: response assessment in neuro-oncology working group. *J Clin Oncol*. 2010;28(11):1963–72.
- Hygino da Cruz LC, Jr, Rodriguez I, Domingues RC, Gasparetto EL, Sorensen AG: Pseudoprogression and pseudoresponse: imaging challenges in the assessment of posttreatment glioma. *AJNR American journal of neuroradiology* 2011, 32(11):1978–1985.
- Kumar AJ, Leeds NE, Fuller GN, Van Tassel P, Maor MH, Sawaya RE, Levin VA: Malignant gliomas: MR imaging spectrum of radiation therapy- and chemotherapy-induced necrosis of the brain after treatment. *Radiology*. 2000;217(2):377–84.
- Qian X, Tan H, Zhang J, Zhao W, Chan MD, Zhou X: Stratification of pseudoprogression and true progression of glioblastoma multiforme based on

- longitudinal diffusion tensor imaging without segmentation. *Med Phys*. 2016;43(11):5889.
7. Ellingson BM, Wen PY, Cloughesy TF. Modified Criteria for Radiographic Response Assessment in Glioblastoma Clinical Trials. *Neurotherapeutics: the journal of the American Society for Experimental NeuroTherapeutics*. 2017;14(2):307–20.
 8. Qu J, Qin L, Cheng S, Leung K, Li X, Li H, Dai J, Jiang T, Akgoz A, Seethamraju R, et al. Residual low ADC and high FA at the resection margin correlate with poor chemoradiation response and overall survival in high-grade glioma patients. *Eur J Radiol*. 2016;85(3):657–64.
 9. Swiderska Z, Markiewicz T, Grala B, Slodkowska J. Hot-spot selection and evaluation methods for whole slice images of meningiomas and oligodendrogliomas. Conference proceedings : Annual International Conference of the IEEE Engineering in Medicine and Biology Society IEEE Engineering in Medicine and Biology Society Annual Conference. 2015;2015:6252–6.
 10. Yoo RE, Choi SH. Recent Application of Advanced MR Imaging to Predict Pseudoprogression in High-grade Glioma Patients. *Magn Reson Med Sci*. 2016;15(2):165–77.
 11. Yun TJ, Park CK, Kim TM, Lee SH, Kim JH, Sohn CH, Park SH, Kim IH, Choi SH. Glioblastoma treated with concurrent radiation therapy and temozolomide chemotherapy: differentiation of true progression from pseudoprogression with quantitative dynamic contrast-enhanced MR imaging. *Radiology*. 2015;274(3):830–40.
 12. Huang YQ, Liang CH, He L, Tian J, Liang CS, Chen X, Ma ZL, Liu ZY. Development and Validation of a Radiomics Nomogram for Preoperative Prediction of Lymph Node Metastasis in Colorectal Cancer. *J Clin Oncol*. 2016;34(18):2157–64.
 13. Horvat N, Veeraraghavan H, Khan M, Blazic I, Zheng J, Capanu M, Sala E, Garcia-Aguilar J, Gollub MJ. MR Imaging of Rectal Cancer: Radiomics Analysis to Assess Treatment Response after Neoadjuvant Therapy. 2018;287(3):833–43.
 14. Tian Q, Yan LF, Zhang X: Radiomics strategy for glioma grading using texture features from multiparametric MRI. 2018.
 15. Gillies RJ, Kinahan PE, Hricak H. Radiomics: Images Are More than Pictures, They Are Data. *Radiology*. 2016;278(2):563–77.
 16. Cha J, Kim ST, Kim HJ, Kim BJ, Kim YK, Lee JY, Jeon P, Kim KH, Kong DS, Nam DH. Differentiation of tumor progression from pseudoprogression in patients with posttreatment glioblastoma using multiparametric histogram analysis. *AJNR Am J Neuroradiol*. 2014;35(7):1309–17.
 17. Song YS, Choi SH, Park CK, Yi KS, Lee WJ, Yun TJ, Kim TM, Lee SH, Kim JH, Sohn CH, et al. True progression versus pseudoprogression in the treatment of glioblastomas: a comparison study of normalized cerebral blood volume and apparent diffusion coefficient by histogram analysis. *Korean journal of radiology*. 2013;14(4):662–72.
 18. Hu X, Wong KK, Young GS, Guo L, Wong ST. Support vector machine multiparametric MRI identification of pseudoprogression from tumor recurrence in patients with resected glioblastoma. *Journal of magnetic resonance imaging : JMIR*. 2011;33(2):296–305.
 19. Abdulla S, Saada J, Johnson G, Jefferies S, Ajithkumar T. Tumour progression or pseudoprogression? A review of post-treatment radiological appearances of glioblastoma. *Clin Radiol*. 2015;70(11):1299–312.
 20. Yushkevich PA, Yang G, Gerig G. ITK-SNAP: An interactive tool for semi-automatic segmentation of multi-modality biomedical images. Conference proceedings : Annual International Conference of the IEEE Engineering in Medicine and Biology Society IEEE Engineering in Medicine and Biology Society Annual Conference. 2016;2016:3342–5.
 21. Tagliamonte SA, Baayen RH. Models, forests and trees of York English: Was/were variation as a case study for statistical practice. *Language Variation & Change*. 2012;24(2):135–78.
 22. Hao M, Wang Y, Bryant SH. An efficient algorithm coupled with synthetic minority over-sampling technique to classify imbalanced PubChem BioAssay data. *Anal Chim Acta*. 2014;806:117–27.
 23. Suh HB, Choi YS: Primary central nervous system lymphoma and atypical glioblastoma: Differentiation using radiomics approach. 2018.
 24. Chu H, Lin X, He J, Pang P, Fan B, Lei P, Guo D, Ye C: Value of MRI Radiomics Based on Enhanced T1WI Images in Prediction of Meningiomas Grade. *Academic radiology* 2020.
 25. Coroller TP, Bi WL, Huynh E, Abedalthagafi M, Aizer AA, Greenwald NF, Parmar C, Narayan V, Wu WW, Miranda de Moura S et al: Radiographic prediction of meningioma grade by semantic and radiomic features. *PLoS one* 2017, 12(11):e0187908.
 26. Delgado-Lopez PD, Rinones-Mena E, Corrales-Garcia EM. Treatment-related changes in glioblastoma: a review on the controversies in response assessment criteria and the concepts of true progression, pseudoprogression, pseudoresponse and radionecrosis. *Clinical & Translational Oncology : official publication of the Federation of Spanish Oncology Societies and of the National Cancer Institute of Mexico*. 2018;20(8):939–53.
 27. Li Y, Qian Z, Xu K, Wang K, Fan X, Li S, Jiang T, Liu X, Wang Y. MRI features predict p53 status in lower-grade gliomas via a machine-learning approach. *NeuroImage Clinical*. 2018;17:306–11.
 28. Nie K, Shi L, Chen Q, Hu X, Jabbour SK, Yue N, Niu T, Sun X. Rectal Cancer: Assessment of Neoadjuvant Chemoradiation Outcome based on Radiomics of Multiparametric MRI. *Clinical cancer research : an official journal of the American Association for Cancer Research*. 2016;22(21):5256–64.
 29. Liu Z, Zhang XY, Shi YJ, Wang L, Zhu HT, Tang Z, Wang S, Li XT, Tian J, Sun YS. Radiomics Analysis for Evaluation of Pathological Complete Response to Neoadjuvant Chemoradiotherapy in Locally Advanced Rectal Cancer. *Clinical cancer research : an official journal of the American Association for Cancer Research*. 2017;23(23):7253–62.
 30. Artzi M, Liberman G, Nadav G, Blumenthal DT, Bokstein F, Aizenstein O, Ben Bashat D. Differentiation between treatment-related changes and progressive disease in patients with high grade brain tumors using support vector machine classification based on DCE MRI. *J Neurooncol*. 2016;127(3):515–24.
 31. Jang BS, Jeon SH, Kim IH, Kim IA. Prediction of Pseudoprogression versus Progression using Machine Learning Algorithm in Glioblastoma. *Scientific reports*. 2018;8(1):12516.
 32. Louis DN, Perry A, Reifenberger G, von Deimling A, Figarella-Branger D, Cavenee WK, Ohgaki H, Wiestler OD, Kleihues P, Ellison DW. The 2016 World Health Organization Classification of Tumors of the Central Nervous System: a summary. *Acta Neuropathol*. 2016;131(6):803–20.
 33. Kanas VG, Zacharaki EI, Thomas GA, Zinn PO, Megalooikonomou V, Colen RR. Learning MRI-based classification models for MGMT methylation status prediction in glioblastoma. *Comput Methods Programs Biomed*. 2017;140:249–57.

Publisher's Note

Springer Nature remains neutral with regard to jurisdictional claims in published maps and institutional affiliations.